Journal for Multiscale Computational Engineering, x(x): 1–30 (2021)

HIERARCHICAL RVE-BASED MULTISCALE MODELLING OF NON-LINEAR HETEROGENEOUS MATERIALS USING THE FINITE VOLUME METHOD

Ke Wu,[1] Željko Tuković,[2] Philip Cardiff,[1] & Alojz Ivanković[1,*]

[1]*I-Form Centre Advanced Manufacturing Research Centre, School of Mechanical and Materials Engineering, University College Dublin*

[2]*Faculty of Mechanical Engineering and Naval Architecture, University of Zagreb*

*Address all correspondence to: Alojz Ivanković, I-Form Centre Advanced Manufacturing Research Centre, School of Mechanical and Materials Engineering, University College Dublin, E-mail: alojz.ivankovic@ucd.ie

This paper describes the development of a hierarchical multiscale procedure within the finite volume OpenFOAM framework for modelling the mechanical response of non-linear heterogeneous solid materials. This is a first development of hierarchical multiscale model for solid mechanics using the finite volume discretisation method. In this computational procedure the information is passed between the macro and micro scales using representative volume elements (RVE), allowing for general, non-periodic microstructures to be considered. An RVE with the prescribed microstructural features is assigned to each computational point. The overall macro response accounts for the microstructural effects through the coupling of macro and micro scales, i.e., the macro deformation gradient is passed to the RVE and in turn, the homogenised micro stress-strain response is passed back to the macro scale. The incremental total Lagrangian formulation is used to represent the equilibrium state of the solid domain at both scales and its integral equilibrium equation is discretised using the cell-centred (colocated) finite volume (FV) method in OpenFOAM. The verification of the model is demonstrated using both 2D and 3D simulations of perforated elastic-plastic plates subjected to tensile loading.

KEY WORDS: *multiscale modelling, finite volume method, RVE, heterogeneous material, OpenFOAM*

1543–1649/17/$35.00

1. INTRODUCTION

Multiscale computational modelling allows for bridging a wide ranges of spatial and temporal scales; it is becoming increasingly popular in many scientific domains where multiscale phenomena and interactions across the scales have pronounced effects on the macro response (Horstemeyer, 2009; Matouš et al., 2017; Salciccioli et al., 2011). These range from the study of protein conformational dynamics to multiphase processes in, for example, granular media or haemodynamics, from nuclear reactor physics to astrophysics (Karabasov et al., 2014), or more recently to modelling of membranes used for parachutes in (Avery et al., 2021). Of course, one can attempt to avoid using multiscale modelling by simply averaging microstructural effects over the entire macro scale, which is the most common approach, or by discretising the entire macro domain with microstructural details. However, in many cases these could be either oversimplification or prohibitively expensive, hence the necessity for multiscale modelling. The decision to pursue a multiscale approach involves a trade-off between increased model fidelity with the added complexity, and the corresponding reduction in precision and increase in uncertainty.

The current work, although developed for general applications, is motivated by Additive Manufacturing (AM), a promising advanced manufacturing technology to directly build up objects layer by layer from 3D virtual prototypes. The increasing importance of multiscale modelling has been demonstrated in AM (Markl and Krner, 2016; Perić et al., 2010; Yashchuk, 2018). Numerous past reviews (Fish, 2006, 2013) have discussed the advantages that can be achieved by multiscale approaches. It is believed that multiscale computations will play a critical role in future nano-technology and materials genome research. Additionally, any computational platform able to encompass numerical procedures for AM modelling also requires efficient, advanced multi-physics and multi-CPU capabilities. OpenFOAM, an open-source computational library, has therefore been chosen in the current work.

The development of many multiscale models begins with recognition that a given assumption, such as the use of a particular constitutive equation, is inadequate for some important range of material response. The mathematical description of material behaviour consists of two types of equations: those that directly reflect physical laws, and those that do not. In general, spatial multiscale modelling is classified into two categories: information passing and concurrent or embedded (de Borst and Ramm, 2011). In the concurrent approach involving the direct simulation of fine-scale behaviour, multiple scales are solved simultaneously or concurrently within a single spatial domain where microstructural details are directly meshed in. This approach is attractive for multiscale material systems either when scale separation does not exist or when the quantities of interest are at a fine scale, for example a crack propagation. This method assumes that the fine-scale model including its geometry is known either from direct measurements or from reconstruction in a portion of the problem domain. The latter one is a promising strategy for reducing the cost

of a fine-scale simulation (such as a molecular dynamics computation) by limiting the fine-scale representation to a small subregion of the full domain while using a less computationally demanding coarse-scale representation for the remaining material. The most well-known of such approaches is the quasi-continuum (QC) method (Tadmor et al., 1996), which couples a molecular dynamics region with a surrounding finite-element representation through a one-to-one match between atoms and finite-element nodes at the interface. Related techniques (Badia et al., 2007; Wagner and Liu, 2003; Xiao and Belytschko, 2004) vary the form of the interface, but most appeal either to a partitioning of the total system energy between the two domains or matching of forces across the boundary to formally derive the coupled system equations. On the other hand, the information passing methods are based on scale infusion where the response of a resolved fine scale is infused into a coarse scale. Information passing methods, which link discrete scales (electronic structure, atomistic, coarse-grained atomistic) and continuum scales (material constituents and components) (Fish et al., 2021) have been proven effective when considering materials whose structure can be divided into multiple scales with each scale having its unique characteristics, which collectively define the macro behaviour (Zeng and Qin, 2018). This approach is widely used, and selected examples from the literature include the prediction of the evolution of interfaces during welding (Tong et al., 2012a,b), the analysis of vapour pressure and void volume fraction evolution in porous polymers (Guo et al., 2015), and the bridging between molecular dynamics and continuum mechanics (Lee et al., 2017). For nonlinear history-dependent problems, information passing methods for atomistic or continuum media would have had little practical impact due to the enormous computational complexity involved. Thus, reduced-order models have been actively studied. Some important reduced-order methods include the Voronoi cell method (Ghosh and Moorthy, 1995), spectral method (Aboudi, 1982), network approximation method (Berlyand and Kolpakov, 2001), fast Fourier transforms (Moulinec and Suquet, 1998), mesh-free reproducing kernel particle method (Chen et al., 1996), finite-volume direct-averaging micromechanics (Cavalcante et al., 2011), transformation field analysis (Dvorak, 1990), methods of cells (Paley and Aboudi, 1992), methods based on control theory including balanced truncation (Moore, 1981), optimal Hankel norm approximation (Glover, 1984), proper orthogonal decomposition (Krysl et al., 2001; Yvonnet and He, 2007), data-driven-based reduced-order methods (Bhattacharjee and Matouš, 2016; Fish et al., 2018; Le et al., 2015), and non-uniform transformation field methods (Fritzen and Böhlke, 2011; Michel and Suquet, 2004). Principally, the multiscale simulations could be based on a combination of these two categories, using concurrent and information passing methods in a hybrid way. This rarely studied approach may include information passing methods for weakly coupled scales while the concurrent method is applied to strongly coupled scales where loss of localisation (such as formation of cracks, voids, and shear bands) and smearing due to homogenisation becomes inadequate.

As customary in stress analysis, the finite element (FE) method has been applied in most of the multiscale modelling of heterogeneous materials (including aforementioned multiscale references). For example, FE^2, a multilevel finite element approach is proposed to account for heterogeneities in the behaviour between a fibre and a matrix (Feyel and Chaboche, 2000), whose constitutive equations are obtained by solving boundary value problems on the micro scale and homogenising the computed properties. An improved version was developed to address the limitations related to discontinuities in the analysis domain (Kouznetsova et al., 2002). Another example includes modelling of cracks where the extended finite element method (XFEM) is used to incorporate discontinuities at the macro-scale (Belytschko and Black, 1999; Moes et al., 1999). Many other examples of the application of multiscale finite element methods can be found in the literature, for example, as reviewed in (Fish, 2013).

The application of the finite volume method has largely been limited to modelling of microstructure type problems using RVEs and unit cell approaches. A recent review paper titled *Thirty Years of the Finite Volume Method for Solid Mechanics* (Cardiff and Demirdžić, 2021), lists over seventy references in the field, mainly from research group led by Ivankovic (Alveen et al., 2014; Carolan et al., 2015; Leonard et al., 2012; McNamara et al., 2014, 2015) and Aboudi & Pindera (Aboudi, 1982, 2004; Aboudi et al., 1999; Cavalcante et al., 2011, 2012). The only true multiscale development in FV using the concurrent or embedded approach is reported in (Alveen et al., 2014, 2015). The current hierarchical multiscale FV approach follows from the initial FV work (Tuković et al., 2019) and is based on principles presented in (Fish, 2013). The Representative Volume Element (RVE) is used at the micro scale to statistically represent the microstructure of the material at each computational point of the macro scale. The coupling between the scales is achieved by passing deformation gradients from the computational points to the corresponding RVEs. The resulting homogenised micro stress-strain fields are passed back to the computational points at the macro scale. For the material model, a hyper-elasto-plastic model has been adopted from (Cardiff et al., 2016) for validation purposes, but any material model can be used.

2. MULTISCALE APPROACH – INFORMATION PASSING

The information passing method, also known as the hierarchical approach, has been employed in this work. This method, which is an alternative to concurrent or embedded methods, requires the use of an RVE to represent microstructural features on smaller scales. The RVE should accommodate enough information about the microstructure, while its dimensions should be smaller than the macroscopic dimensions in order to satisfy the concept of scale separation (Mirkhalaf et al., 2016). The first step in this approach is to approximate the problem with a coarse representation of the underlying macroscale domain. Then, a pre-specified RVE is assigned to each material point on the

macroscale. In this work, the microstructural features are represented as voids for simplicity, following the previous FEA work (Fish, 2013). In Fig. 1, the characteristic length l_μ of the RVE is much smaller than the characteristic length l of the macro continuum. The domain Ω_μ of the RVE consists of two components: solid part Ω_μ^s and void part Ω_μ^v. The following gives a short overview of the multiscale modelling and homogenisation methods for nonlinear problems based on (Geers et al., 2017) but adjusted to be applied with the FV method.

2.1 Macroscale problem

At the macroscopic scale, the deformation is governed by the momentum conservation law, which in the absence of inertia and body forces can be expressed in term of the Cauchy stress tensor $\boldsymbol{\sigma}$ as:

$$\oint_\Gamma \boldsymbol{n} \cdot \boldsymbol{\sigma} \, \mathrm{d}\Gamma = 0, \tag{1}$$

FIG. 1: Macro-continuum with a locally assigned RVE.

or in terms of the first Piola–Kirchhoff stress tensor $\boldsymbol{P}$ as:

$$\oint_{\Gamma_0} \boldsymbol{n}_0 \cdot \boldsymbol{P}^{\mathrm{T}} \, \mathrm{d}\Gamma_0 = 0, \tag{2}$$

where Γ is the boundary surface of the macro body in the current configuration, $\boldsymbol{n}$ is the unit normal to Γ, Γ_0 is the boundary surface of the macro body in the initial configuration and $\boldsymbol{n}_0$ is the unit normal to Γ_0. To close this boundary value problem, a constitutive relation between the stress and kinematic quantities needs to be defined. Instead of assuming a constitutive equation in a closed form, the computational homogenisation (CH) technique extracts the constitutive response numerically from the detailed computational analysis of a microstructural RVE.

FIG. 2: Computational homogenization scheme.

Deformation of the macro-continuum is described by the macroscopic deformation gradient tensor

$$\boldsymbol{F} = (\nabla_0 \boldsymbol{x})^{\mathrm{T}} = \left(\frac{\partial \boldsymbol{x}}{\partial \boldsymbol{X}}\right)^{\mathrm{T}} = \mathbf{I} + \left(\frac{\partial \boldsymbol{u}}{\partial \boldsymbol{X}}\right)^{\mathrm{T}} = \mathbf{I} + (\nabla_0 \boldsymbol{u})^{\mathrm{T}}, \tag{3}$$

where ∇_0 is the gradient operator with respect to the reference configuration, $\mathbf{I}$ is the second-order unit tensor, $\boldsymbol{x}$ and $\boldsymbol{X}$ denote the position vectors in the current and reference configurations, respectively, and $\boldsymbol{u} = \boldsymbol{x} - \boldsymbol{X}$ is the macro-scale displacement vector.

The CH framework is schematically illustrated in Fig. 2. The macroscopic deformation gradient tensor $\boldsymbol{F}$ is calculated for every material point of the macroscale structure (e.g., the cell-centres of the macroscopic mesh within a collocated finite volume environment). Next, $\boldsymbol{F}$ is used to formulate the boundary conditions imposed on the RVE assigned to the considered point. Upon the solution of the boundary value problem for the RVE, the macroscopic stress tensor $\boldsymbol{P}$ is obtained, thus providing the numerical stress-deformation relationship at the macroscopic point.

2.2 Microscale problem

The physical and geometrical properties of the microstructure are identified by an RVE. Here, it is assumed that an appropriate RVE, capable of capturing relevant microscale physics and fluctuations, has been selected. In accordance with the separation of scales principle, the RVE should be much smaller than the characteristic length of the relevant macroscopic field variation, but sufficiently larger than micro fluctuations. If this condition holds, then any change in the macroscopic field variables will immediately be accommodated at the RVE scale, and the RVE problem is quasi-static even though the macroscopic problem can be transient (Geers et al., 2017).

Deformation of the microscale continuum (RVE) is linked with the deformation of the macroscale continuum by decomposing the full displacement of the RVE into homogenous and micro-fluctuation part as follows

$$\boldsymbol{u}_\mu = \bar{\boldsymbol{u}}_\mu + \tilde{\boldsymbol{u}}_\mu, \tag{4}$$

where the microfluctuation displacement $\tilde{\boldsymbol{u}}_\mu$ represents the local fine scale contribution superimposed on to the macroscale homogenous deformation determined by macroscopic deformation gradient $\boldsymbol{F}$,

$$\bar{\boldsymbol{u}}_\mu = (\boldsymbol{F} - \mathbf{I}) \cdot \boldsymbol{X}_\mu. \tag{5}$$

From (4), the microscale deformation gradient tensor is defined as

$$\boldsymbol{F}_{\mu} = \mathbf{I} + (\nabla_{0\mu}\boldsymbol{u})^{\mathrm{T}} = \boldsymbol{F} + (\nabla_{0\mu}\tilde{\boldsymbol{u}}_{\mu})^{\mathrm{T}}. \tag{6}$$

Relations (4) and (6) are valid for every point at the microscale, with the first terms known for a given macro-scale deformation tensor $\boldsymbol{F}$. The microfluctuation $\tilde{\boldsymbol{u}}_{\mu}$ will be obtained from the solution of the micro-scale boundary value problem.

The equilibrium equation for the RVE in the absence of inertia and body force can be expressed in integral or differential form as follows:

$$\int_{\Gamma_{0\mu}} \boldsymbol{n}_{0\mu} \cdot \boldsymbol{P}_{\mu}^{\mathrm{T}} \, \mathrm{d}\Gamma_{0\mu} = 0 \quad \text{or} \quad \nabla_{0\mu} \cdot \boldsymbol{P}_{\mu}^{\mathrm{T}} = 0, \tag{7}$$

where $\boldsymbol{P}_{\mu}$ is the microscale first Piola–Kirchhoff stress tensor, $\Gamma_{0\mu}$ is the boundary surface of the RVE in the initial configuration and $\boldsymbol{n}_{0\mu}$ is the unit normal to $\Gamma_{0\mu}$. The material behaviour of each microstructural constituent is assumed to be known and described by constitutive laws that specify a stress-strain relation. In this study, a hyper-elasto-plastic deformation of the matrix material of the RVE has been defined by the hyper-elasto-plastic material model, where the Kröner-Lee multiplicative decomposition of the deformation gradient together with a rate-independent isotropic hyperelastoplastic constitutive relation (Simo and Hughes, 2006) is employed. The Kirchhoff stress $\boldsymbol{\tau}_{\mu} = J_{\mu}\boldsymbol{\sigma}_{\mu}$ is given in terms of an uncoupled volumetric-deviatoric relation (Cardiff et al., 2016):

$$\boldsymbol{\tau}_{\mu} = J_{\mu}\boldsymbol{\sigma}_{\mu} = \frac{K_{\mu}}{2}(J_{\mu}^{2} - 1)\mathbf{I} + G_{\mu} \, \mathrm{dev}[\bar{\boldsymbol{b}}_{\mu}^{e}], \tag{8}$$

where K_{μ} is the bulk modulus, G_{μ} is the shear modulus, J_{μ} is the Jacobian (determinant of the deformation gradient) and $\bar{\boldsymbol{b}}_{\mu}^{e}$ is the volume-preserving component of the left Cauchy-Green deformation tensor. The classical Mises-Huber J_2 yield condition, formulated in terms of Kirchhoff stress tensor, is employed (Simo and Hughes, 2006):

$$f(\boldsymbol{\tau}_{\mu}, \epsilon^{p,eq}) = ||\mathrm{dev}[\boldsymbol{\tau}_{\mu}]|| - \sqrt{\frac{2}{3}}[\sigma_{Y}(\epsilon^{p,eq})] \leqslant 0, \tag{9}$$

where the yield stress σ_Y is a function of equivalent plastic strain $\epsilon^{p,eq}$. More details related to the implementation of the hyperelastoplastic constitutive relation in the context of the finite volume method can be found in (Cardiff et al., 2016).

The microscopic equilibrium equation (7) requires boundary conditions. The essential step in the CH methodology is the derivation of RVE boundary conditions from the scale transition relations, as is discussed in the following section.

2.3 Macro-to-micro coupling

A commonly used scale transition procedure for establishing the macro-to-micro coupling is based on kinematic averaging, where the volume average of the micro-scale deformation gradient tensor $\boldsymbol{F}_\mu$ has to be equal to the corresponding macro-scale deformation gradient tensor $\boldsymbol{F}$,

$$\boldsymbol{F} = \frac{1}{\Omega_{0\mu}} \int_{\Omega_{0\mu}} \boldsymbol{F}_\mu \, \mathrm{d}\Omega_\mu, \tag{10}$$

where Ω_μ is the RVE volume in the reference configuration. Insertion of equation (6) into the right-hand side of the scale transition relation (10) yields

$$\begin{aligned} \frac{1}{\Omega_\mu} \int_{\Omega_\mu} \boldsymbol{F}_\mu \mathrm{d}\Omega_\mu &= \boldsymbol{F} + \frac{1}{\Omega_{0\mu}} \int_{\Omega_{0\mu}} (\nabla_{0\mu} \tilde{\boldsymbol{u}}_\mu)^{\mathrm{T}} \mathrm{d}\Omega_{0\mu} \\ &= \boldsymbol{F} + \frac{1}{\Omega_{0\mu}} \oint_{\Gamma_{0\mu}} \tilde{\boldsymbol{u}}_\mu \boldsymbol{n}_{0\mu} \mathrm{d}\Gamma_{0\mu}, \end{aligned} \tag{11}$$

where the divergence theorem has been used to transform the volume integral to the integral over the undeformed boundary of the RVE, $\Gamma_{0\mu}$, with outward normal $\boldsymbol{n}_{0\mu}$.

It is clear that the boundary conditions on the RVE must be chosen in such a way that the contribution of the microfluctuation field $\tilde{\boldsymbol{u}}_\mu$ in equation (11) vanishes in order to satisfy the scale transition relation (10). This can be achieved in many ways. Some of the possibilities proposed and used in the literature are listed below:

1. Suppress the micro-fluctuation at the RVE boundary

$$\tilde{\boldsymbol{u}}_\mu = 0, \quad \forall \, \boldsymbol{X}_\mu \in \Gamma_{0\mu}, \tag{12}$$

   while leaving the microstructural fluctuations inside the volume yet undetermined. Using equation (4), the above relation can equivalently be written as

$$\boldsymbol{u}_\mu = (\boldsymbol{F} - \mathbf{I}) \cdot \boldsymbol{X}_\mu. \tag{13}$$

With this condition, the displacements of the RVE boundary are fully prescribed according to the given $\boldsymbol{F}$. These are often termed as *uniform displacement boundary conditions*.

2. For an RVE with geometrically periodic boundary, the boundary can be split in "+" and "-" parts defined by the opposite outward normal vectors at the corresponding points, $\boldsymbol{n}_{0\mu}^{+} = \boldsymbol{n}_{0\mu}^{-}$, and so-called *periodic boundary conditions* can be imposed by requiring the periodicity of the micro-fluctuation field

$$\tilde{\boldsymbol{u}}_{\mu}^{+} = \tilde{\boldsymbol{u}}_{\mu}^{-}. \tag{14}$$

3. Prescribe traction on the RVE boundary according to a given macroscopic stress $\boldsymbol{P}$

$$\boldsymbol{p}_{\mu} = \boldsymbol{P} \cdot \boldsymbol{n}_{0\mu}, \quad \forall\, \boldsymbol{X}_{\mu} \in \Gamma_{0\mu}, \tag{15}$$

These are usually called *uniform traction boundary conditions*.

For a given microstructural RVE size, the periodic boundary conditions are known to provide a better estimation of the overall properties than the mentioned alternatives. The periodic boundary conditions are most frequently used in practice, although the uniform displacement boundary conditions are also often used due to the simplicity of implementation.

2.4 Micro-to-macro transition: Hill–Mandel condition

The micro-to-macro scale transition relation is usually established based on the so-called Hill–Mandel condition or macro-homogeneity condition. This condition requires the volume average of the increment (or variation) of work performed on the RVE to be equal to the increment (or variation) of local work on the macroscale. Formulated in terms of a work conjugated set, that is, the deformation gradient tensor and the first PiolaKirchhoff stress tensor, the Hill–Mandel condition reads,

$$\frac{1}{\Omega_{0\mu}} \int_{\Omega_{0\mu}} \boldsymbol{P}_{\mu} : \delta \boldsymbol{F}_{\mu}^{\mathrm{T}} \, \mathrm{d}\Omega_{0\mu} = \boldsymbol{P} : \delta \boldsymbol{F}^{\mathrm{T}}. \tag{16}$$

Based on the Hill–Mandel condition (16), it is shown in (Geers et al., 2017) that if the RVE boundary conditions (12) and (13) are used, the macroscale first Piola–Kirchhoff stress tensor can be identified as the volume average of the

microscale first Piola–Kirchhoff stress tensor,

$$\boldsymbol{P} = \frac{1}{\Omega_{0\mu}} \int_{\Omega_{0\mu}} \boldsymbol{P}_{\mu} \mathrm{d}\Omega_{0\mu}, \tag{17}$$

and the macroscale Cauchy stress tensor can be calculated using standard continuum mechanics relation,

$$\boldsymbol{\sigma} = \frac{1}{J} \boldsymbol{P} \cdot \boldsymbol{F}^{\mathrm{T}}, \tag{18}$$

where $J = \det(\boldsymbol{F})$ is the Jacobian of the deformation gradient tensor.

The actual choice of the averaging measures: the deformation gradient tensor $\boldsymbol{F}$ and the first Piola-Kirchhoff stress tensor $\boldsymbol{P}$ has been proposed by Hill (1984). This choice is motivated by the fact that these two measures are work conjugated, combined with the observation that their volume averages can be defined in terms of the microstructural quantities on the RVE boundary only. For example, average first Piola–Kirchhoff stress can be calculated as follows:

$$\boldsymbol{P} = \frac{1}{\Omega_{0\mu}} \oint_{\Gamma_{0\mu}} \boldsymbol{p}_{\mu} \boldsymbol{X}_{\mu} \, \mathrm{d}\Gamma_{0\mu}. \tag{19}$$

where $\boldsymbol{p}_{\mu} = \boldsymbol{P}_{\mu} \cdot \boldsymbol{n}_{0\mu}$ is the first Piola-Kirchhoff traction vector.

3. DISCRETISATION OF GOVERNING EQUATION USING THE CELL-CENTRED FV METHOD

As is previously shown, both macro- and micro-scale problems are mathematically described by the equilibrium equations of the equal form:

$$\oint_{\Gamma_0} \boldsymbol{n}_0 \cdot \boldsymbol{P}^{\mathrm{T}} \, \mathrm{d}\Gamma_0 = 0, \tag{20}$$

$$\oint_{\Gamma_0} \boldsymbol{n}_{0\mu} \cdot \boldsymbol{P}_{\mu}^{\mathrm{T}} \, \mathrm{d}\Gamma_{0\mu} = 0. \tag{21}$$

In this study, the equilibrium equation of the macroscale problem (20) is solved for displacement increment:

$$\Delta \boldsymbol{u}^m = \boldsymbol{u}^m - \boldsymbol{u}^{m-1}, \tag{22}$$

while the equilibrium equation of the microscale problem (21) is solved for the increment of displacement fluctuation:

$$\Delta \tilde{\boldsymbol{u}}_{\mu}^m = \tilde{\boldsymbol{u}}_{\mu}^m - \tilde{\boldsymbol{u}}_{\mu}^{m-1}, \tag{23}$$

where superscripts m and $m-1$ represent current and previous loading steps respectively. Finite volume discretisation of the equilibrium equations is described in the continuation only for the macroscale problem.

The second-order accurate cell-centred finite volume method is applied to discretise the solution domain and the governing equations. The spatial computational domain in the initial configuration is divided into a finite number of unstructured control volumes (CV) or cells bounded by convex polygons. Figure 3 shows a typical general convex polyhedral cell with the computational point P located in its centroid and cell volume is Ω_{0P}; N is the centroid of a neighbouring control volume, which shares face f with the current control volume; Γ_{0f} is the area of face f, $\boldsymbol{n}_{0f}$ is the unit normal vector of face f, vector d_f joins P to N, and $\boldsymbol{X}_P$ is the position vector of the cell centre point P. The quasi-time (loading) interval is split into a finite number of loading steps and the equations are solved in a quasi-time-marching manner.

According to the FV discretisation method, the surface integral of Eq. (20) is transformed into a sum of face integrals which are, together with the volume integral, approximated to second-order accuracy using the mid-point rule. The resulting nonlinear discretised counterpart of the equilibrium equation (20) for the control volume $\Omega_{0,P}$ reads (Tuković et al., 2018):

$$\sum_f \boldsymbol{n}_{0f} \cdot \boldsymbol{P}_f^{\mathrm{T}} \, \Gamma_{0f} = 0, \tag{24}$$

where subscript f represents a face-centred values. The face-centre first Piola-Kirchhoff stress tensor $\boldsymbol{P}_f$ is calculated explicitly by linear interpolation of the corresponding cell-centre values. In order to enhance the implicit part of the

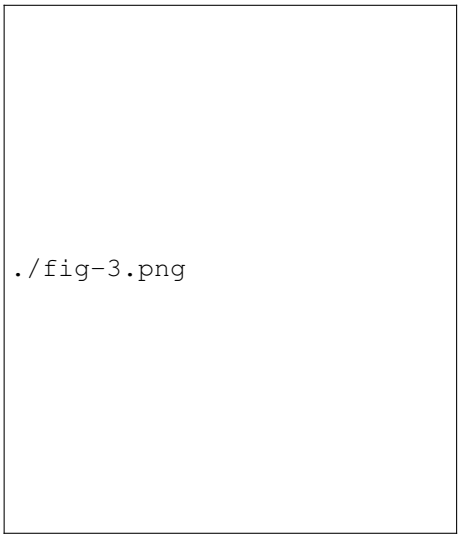

FIG. 3: General convex polyhedral control volume (CV) as an element of the computational mesh representing discretised spatial domain in its initial configuration.

discretised model, the linear Laplace term, which represents a linearisation of the divergence of stress, is introduced to the left and right-hand side of Eq. (24) as follow (Cardiff et al., 2016):

$$\underbrace{\sum_f (K_i)_f \frac{\Delta \boldsymbol{u}_N^m - \Delta \boldsymbol{u}_P^m}{d_{0f}} \Gamma_{0f}}_{\text{linear part (implicit)}} = \underbrace{\sum_f (K_i)_f \frac{\boldsymbol{d}_{0f}}{d_{0f}} \cdot (\nabla_0 \Delta \boldsymbol{u})_f^m \Gamma_{0f} + \sum_f \boldsymbol{n}_{0f} \cdot \left(\boldsymbol{P}_f^m\right)^{\mathrm{T}} \Gamma_{0f}}_{\text{nonlinear part (explicit)}}, \tag{25}$$

where the Laplace term on the left-hand side is treated implicitly while the Laplace term on the right-hand side is explicit. Addition of these terms do not affect the solution, moreover, due to the different computational stencil used for discretisation of implicit and explicit Laplacian terms, the difference between them results in additional numerical diffusion which tends to reduce oscillations of the solution. The diffusion coefficient represented by K_i in the Laplace terms does not influence the final result, but it can have an impact on the stability of the solution procedure; it is given in this study as:

$$K_i = \frac{3}{4} G + K, \tag{26}$$

where K is the bulk modulus, G is the shear modulus of macro-scale continuum. The cell-centred gradient of displacement increment required for evaluation of deformation gradient and explicit Laplacian term is calculated using least–square method (Jasak and Weller, 2000).

Finally, the discretised counterpart of the equilibrium equation (20) for each control volume P in the mesh can be represented in the following form of a linear algebraic equation:

$$a_P \Delta \boldsymbol{u}_P^m + \sum_N a_N \Delta \boldsymbol{u}_N^m = \boldsymbol{b}_P, \tag{27}$$

where a_P is the central (diagonal) coefficient, a_N are the neighbour coefficients representing interactions with neighbour cell-centred unknowns and $\boldsymbol{b}_P$ is the source vector contribution.

The resulting system of equations for the entire computational domain takes the form:

$$[A][\Delta \boldsymbol{u}] = [\boldsymbol{b}], \tag{28}$$

where $[A]$ is the sparse $n \times n$ matrix with weak diagonal dominance, with n being the total number of control volumes. The coefficients a_P are on the diagonal of matrix $[A]$, and coefficients a_N form the matrix off-diagonals. The solution vector $[\Delta \boldsymbol{u}]$ contains the unknown cell-centred displacement increments $\Delta \boldsymbol{u}$, and $[\boldsymbol{b}]$ is the source vector containing the explicitly discretised terms of equilibrium equation and boundary condition contributions. The above system is

solved based on an implicit integration in quasi-time using a segregated solution procedure, which is common in FV Computational Fluid Dynamics (CFD)/Computational Solid Mechanics (CSM), and components of displacement increment are solved in a decoupled manner. The linear system for each displacement increment component is solved by a preconditioned conjugate gradient solver.

As already mentioned, the discretised equilibrium equation (25) is solved iteratively using the fixed-point (Gauss–Seidel) iterative solution procedure, where explicit terms are evaluated using displacement increments from the previous iteration. Specifically, after the new displacement increment field is obtained, new total displacement and deformation gradient are calculated and used to update the first Piola-Kirchoff stress field by solving RVE problem. All implementations have been performed in the open-source C++ toolbox OpenFOAM (Weller et al., 1998) (version foam-extend-4.1) with a solution tolerance set to 10^{-6}. In contrast to the Newton-Raphson methods commonly used in the FE method, the fixed point (Gauss-Seidel) approach shows first order convergence in contrast to the second order convergence of the Newton-Raphson method, however, this disadvantage is mitigated by the fact that the linearised system in the paper is quick to assemble and iteratively solve. Theoretically, a Newton-Raphson method can also be used, but it would require a block-coupled approach for the linearised problem.

The overall macro-micro information passing process depicted in Fig. 1 can be summarised as follows. First, the deformation gradient is calculated at the macro-scale computational points under the specified macro loading conditions and then applied uniformly over its corresponding RVEs. Following the solution of the equilibrium equation (21) for the RVE, the volume-averaged first Piola-Kirchhoff stress tensor from the RVE is passed back to the macro domain and this procedure is repeated within each quasi-time step until convergence. The overall multiscale solution procedure is summarised in Algorithm 1 and Algorithm 2.

Algorithm 1: Solution procedure for the macro-problem

1: **for all** loading steps **do**
2: **while** explicit terms are not converged **do**
3: Momentum equation: assemble and solve in terms of $\Delta \boldsymbol{u}$
4: Calculate cell-centre total deformation gradient $\boldsymbol{F}$
5: Calculate cell-centre first Piola–Kirchhoff stress $\boldsymbol{P}$ by solving RVE-problem {See Algorithm 2}
6: **end while**
7: **end for**

Algorithm 2: Solution procedure for RVE-problem

1: Pass deformation gradient from a macro-cell-centre and use it as a specified average deformation gradient for the RVE-problem
2: **for all** loading steps **do**
3: **while** explicit terms are not converged **do**
4: Momentum equation: assemble and solve in terms of $\Delta\tilde{\boldsymbol{u}}$
5: Calculate cell-centre deformation gradient $\boldsymbol{F}_{\mu}$
6: Calculate cell-centre Cauchy stress $\boldsymbol{\sigma}_{\mu}$ using material model (8)
7: Transform cell-centre Cauchy stress to first Piola–Kirchhoff stress $\boldsymbol{P}_{\mu}$
8: **end while**
9: **end for**

4. NUMERICAL RESULTS

In this numerical section, three sets of examples are presented. The first set of examples focuses on 2D analyses of two elasto-plastic perforated plates, one with a central hole and one without. A comparison with the corresponding single-scale model in the concurrent approach is also included as a benchmark. The second example set is an extension of the plate without a hole case to 3D, where 2D voids become cylinders in 3D. Finally, the third example is a true 3D case where cylindrical voids are replaced by spherical voids. A plate with a thickness of 5 times the side length of the RVE and with each RVE containing a spherical void is considered here. In each case, the plate is loaded in uniaxial tension by applying uniform vertical displacement and the side length of the RVE is kept at $1\ \mathrm{mm}$.

4.1 2D two-scale analysis of a stretching perforated elasto-plastic plate

The stretching of a perforated plate is a widely used benchmark example in computational plasticity and is analysed in this section assuming plane strain conditions (Perić et al., 2010). Two different configurations of perforated plate are selected to examine the accuracy of the newly developed RVE-based multiscale model (Figure 4). The first configuration considers a uniform, perforated plate $10\ \mathrm{mm}$ in width, $18\ \mathrm{mm}$ in length, and containing 180 uniformly distributed voids $0.5\ \mathrm{mm}$ in diameter. The second configuration is the same plate but with the addition of a central hole, $5\ \mathrm{mm}$ in radius, and containing 161 voids. Due to the symmetry, only one-quarter of the plate is considered. The material in all models is assumed to be composed of a von Mises elasto-plastic material with linear strain hardening. Table 1 shows the material properties of an aluminium alloy used in the single-scale simulations and for the RVE in

the two-scale simulations (taken from (Perić et al., 2010)). The material properties for the macro domain in two-scale simulations are obtained from the stress-strain response of the single-scale uniform perforated plate simulations. In the single-scale simulation, a time-dependent uniform displacement is imposed at the top boundary, symmetry boundary conditions are applied at left and bottom boundaries. The right boundary as well as the edge of the central hole are prescribed with traction-free boundary conditions. For the two-scale analysis, the same boundary conditions are applied in the macro region while periodic boundary conditions are applied to the external boundaries of each RVE.

Quadrilateral meshes are generated in ANSYS/ICEM. In the single-scale analysis, the meshes for the perforated plate without/with large central hole are composed of $20,880$ and $18,676$ hexahedral cells respectively (see Figure 5(a)). It should be noted that OpenFOAM uses 3-D meshes, with one cell extruded in the thickness direction, for 2-D

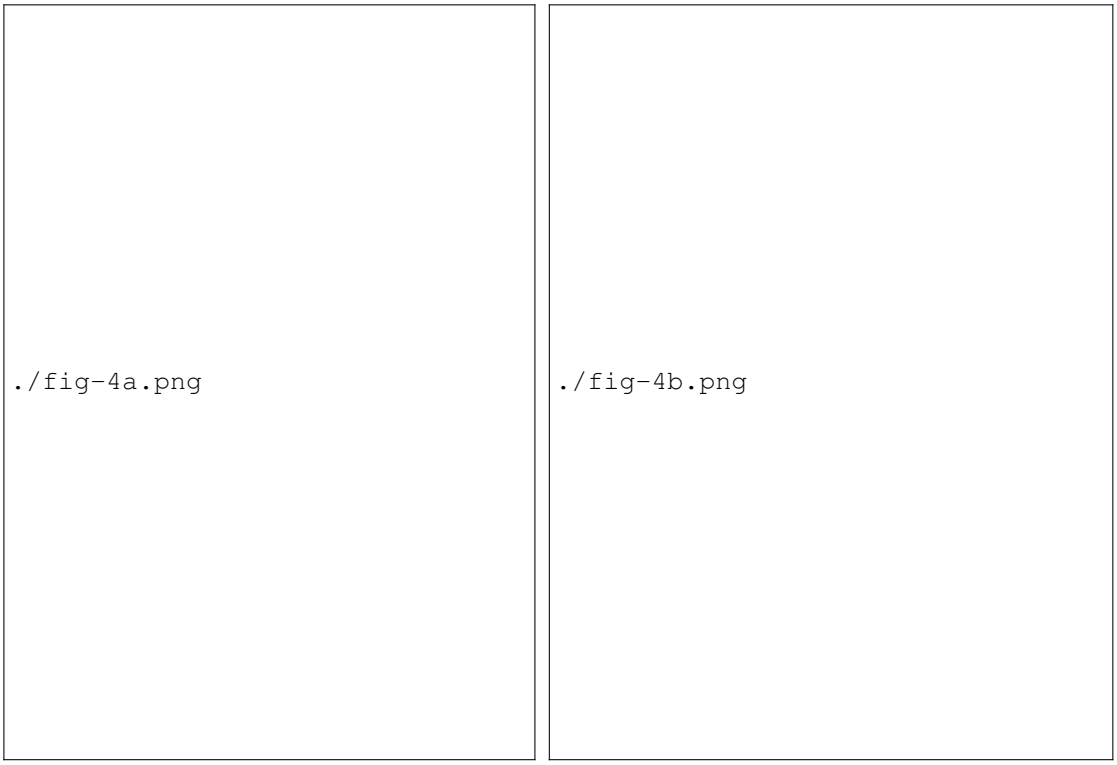

FIG. 4: Configurations of the elasto-plastic perforated plate: (a) uniform plate and (b) plate with central hole

TABLE 1: Material properties of the aluminium elasto-plastic perforated plate

Density (ρ)	$7000\ \mathrm{kg/m^3}$
Young's modulus (E)	$70\ \mathrm{GPa}$
Poisson ratio (ν)	0.2
Yield strength (σ_y)	$243\ \mathrm{MPa}$
Strength hardening (H_P)	$443\ \mathrm{MPa}$

models, hence quadrilateral cells in ICEM are converted to hexahedral cells in OpenFOAM. In contrast to the single-scale analysis, the macro level meshes contain only 180 and 154 hexahedral cells respectively and 116 hexahedral cells for each RVE (see Figure 5(b)). In all cases, mesh density was selected as a compromise between low computational cost and low mesh error.

Figure 6 shows the distribution of the displacement component in the loading (vertical) direction for both 2D configurations at the final loading step. At the macro level, the distribution of displacement resembles that from single-scale analysis. The corresponding distributions of stress component in the loading direction are shown in Figure 7. The stress distribution for the RVE near the bottom-left of the plate is periodic, and as expected, resembles the stress distribution around the voids in the single scale. The stress distribution at the macro scale is the volume average of RVEs or indeed the single scale and shows a close agreement in stress variation through the plate. The accuracy of the stresses at the macro scale predicted from two-scale model depends on the heterogeneity of the microstructure. At small strains, heterogeneity coincides with features in the initial microstructure (e.g., void in RVE) and additional heterogeneity in the microstructure arises from gradients of the deformation at larger strain. It is expected that the overall level of error grows substantially as plastic deformation accumulates spatially. The efforts to mitigate the error can be made by increasing the mesh resolution to improve the stress prediction.

Figure 8 compares the results from the exact single-scale analysis with those from the newly developed two-scale multi-scale analyses for both configurations of the perforated plate. The average top edge traction, calculated as the total forces at the top edge divided by the total deformed surface area, is plotted against prescribed top edge displacement for all cases considered. The two-scale predictions are in good agreement with the results obtained from the single-scale analysis. A minor discrepancy ($< 5\%$) develops near the onset of yielding and remains present in the plastic region. This is caused by the boundary effect at the macro scale, where the traction boundary condition is applied to the right boundary of the perforated plates as well as along the edge of the central hole. The periodic conditions used to find the incremental fluctuation in the RVEs are strictly applicable only inside the body, and the validity of periodic conditions is somewhat questionable in the region near to traction-free boundaries (Kanouté et al., 2009). Overall, periodic boundary conditions applied to the RVEs result in good agreement with the results obtained from the single-scale analysis.

4.2 Pseudo 3D two-scale analysis of a stretching perforated elasto-plastic plate

The 2D simulation of the perforated plate without a central hole from the previous section is extended into a pseudo-3D case by extruding the plate in the out-of-plane direction. The plate is extruded to a thickness of 5 mm, which is

5 times the side length of the RVE prescribed as $1\ \mathrm{mm}$ (Figure 9). By doing so, the voids in the single-scale analysis became cylindrical holes with $0.5\ \mathrm{mm}$ diameter (Figure 9(a)), while the RVE in the two-scale simulations takes a cubic shape with a cylindrical hole at its centroid (Figure 9(c)). Traction-free boundary condition is applied to the back surface of the plate and its front surface is assigned with a symmetry boundary condition, resulting in the plane-stress dominant conditions through the plate thickness. Material properties and loading conditions are identical to the previous example. The mesh for single scale-case consists of 104,400 hexahedral cells, i.e. 5 times the corresponding 2D case. In the two-scale analysis, the mesh at the macro level is composed of 900 hexahedral cells, the number of cells for the RVEs remains unchanged, but the quantity of RVEs is increased from 180 to 900.

Figure 10 presents predicted stress-displacement curves from 2D plane strain (blue and purple lines) and 3D simulations (yellow and green lines). As expected, the 3D results show a lower modulus and lower average yielding traction, as the cases are plane-stress in nature. As in 2D simulations, the 3D results obtained from single-scale analysis and two-scale analysis are in good agreement. Due to the evenly periodic distribution of cylindrical voids representing the actual heterogeneity, periodic boundary conditions applied to RVEs are appropriate.

4.3 3D two-scale analysis of a stretching perforated elasto-plastic plate

This final test case extends the previous pseudo-3D example into a full 3D case by considering a plate with 5 spherical voids of $0.5\ \mathrm{mm}$ diameter, distance $1\ \mathrm{mm}$ apart, uniformly distributed across the thickness; the remaining dimensions of the plate are the same as in the previous example. The plate contains a total of 900 uniformly distributed spherical voids (18 vertically, 10 horizontally and 5 through thickness), as shown in Figures 11(a) and (b). The total thickness of the plate, $5\ \mathrm{mm}$, is taken as 5 times the side length of the RVE, hence each RVE shown in Figures 11 (c) and (d) has a spherical void in its centroid. In this case, deformation in the thickness direction is allowed by applying symmetry boundary condition on the plate front side and stress-free boundary condition on the plate back side while keeping other boundary conditions the same as in the previous two examples. Material properties and loading conditions are the same as in the previous examples. Due to the full 3D nature of the problem, the total number of hexahedral cells in the single-scale analysis has increased to 842,400.

Figure 12 presents the stress-displacement curves from the single-scale and two-scale multi-scale analyses of the 3D perforated plate with spherical voids. The agreement between the predictions is good. Similar to 2D and pseudo 3D cases, the minor discrepancy ($< 5\%$) also develops in the full 3D case near the onset of yielding and remains present in the post-yield region.

5. CONCLUSIONS

A novel RVE-based information passing multiscale model has been developed using an FV discretisation method in the OpenFOAM software. The model is applied to an elastic-plastic material within an incremental total Lagrangian framework. This is the first development of an FV based hierarchical multiscale procedure for solid mechanics. The RVE is introduced to allow for a smooth micro-to-macro transition resulting in a homogenisation-based constitutive relation. Periodic boundary conditions have been used to solve the boundary value problem of the RVE. The developed procedures were verified against single-scale simulations on plate-like samples containing microstructural details, i.e. voids, for both 2D and 3D cases. The RVE-based multiscale model predictions were found to be in good agreement with single-scale results. The minor discrepancy ($< 5\%$) between the benchmark and multi-scale results were attributed to the use of periodic boundary conditions in the RVE which are not strictly appropriate near the macro-scale traction boundaries. This discrepancy was found to be in the range of published values (e.g. [8]) and within the acceptable tolerance. Future work will be focused on adaptive hierarchical models where RVEs are called at selected material points within the macro-scale based on predefined conditions and on developing hybrid approaches which combine information passing and concurrent approaches. Of particular interest is the application of the model to predicting process-structure-property relationships in additive manufacturing.

ACKNOWLEDGMENTS

This publication has emanated from research conducted with the financial support of Science Foundation Ireland under Grant number 16/RC/3872. For the purpose of Open Access, the authors have applied a CC BY public copyright licence to any Author Accepted Manuscript version arising from this submission. Additionally, the third author gratefully acknowledges financial support from the Irish Research Council through the Laureate programme, grant number IRCLA/2017/45, and from Bekaert through the University Technology Centre (UTC phases I and II) at UCD.

APPENDIX A. COEFFICIENTS OF DISCRETISED MACRO-SCALE EQUILIBRIUM EQUATION

As is described in Section 3, equation (25) obtained by discretisation of the macroscale equilibrium equation (20) for the control volume P of the macro-scale mesh using collocated FVM, can be represented by the linear algebraic equation (27). The central (diagonal) coefficient of this equation is defined as follows:

$$a_P = -\sum_f \frac{(K_i)_f}{d_{0f}} \Gamma_{0f}, \tag{A.1}$$

while the off-diagonal (neighbour) coefficients read:

$$a_N = \frac{(K_i)_f}{d_{0f}} \Gamma_{0f}. \tag{A.2}$$

Finally, right hand side of the linear equation contains explicitly discretised terms of the equilibrium equation:

$$\boldsymbol{b}_P = \sum_f (K_i)_f \frac{\boldsymbol{d}_{0f}}{d_{0f}} \cdot (\nabla_0 \Delta \boldsymbol{u})_f^m \, \Gamma_{0f} + \sum_f \boldsymbol{n}_{0f} \cdot \left(\boldsymbol{P}_f^m\right)^{\mathrm{T}} \, \Gamma_{0f}. \tag{A.3}$$

REFERENCES

Aboudi, J., A continuum theory for fiber-reinforced elastic-viscoplastic composites, *International Journal of Engineering Science*, vol. **20**, no. 5, pp. 605–621, 1982.

Aboudi, J., The generalized method of cells and high-fidelity generalized method of cells micromechanical models—a review, *Mechanics of Advanced Materials and Structures*, vol. **11**, no. 4-5, pp. 329–366, 2004.

Aboudi, J., Pindera, M.J., and Arnold, S., Higher-order theory for functionally graded materials, *Composites Part B: Engineering*, vol. **30**, no. 8, pp. 777–832, 1999.

Alveen, P., McNamara, D., Carolan, D., Murphy, N., and Ivanković, A., Analysis of two-phase ceramic composites using micromechanical models, *Computational Materials Science*, vol. **92**, pp. 318–324, 2014.

Alveen, P., McNamara, D., Carolan, D., Murphy, N., and Ivanković, A., The influence of microstructure on the fracture properties of polycrystalline cubic boron nitride, *Computational Materials Science*, vol. **109**, pp. 115–123, 2015.

Avery, P., Huang, D.Z., He, W., Ehlers, J., Derkevorkian, A., and Farhat, C., A computationally tractable framework for nonlinear dynamic multiscale modeling of membrane woven fabrics, *International Journal for Numerical Methods in Engineering*, vol. **122**, no. 10, pp. 2598–2625, 2021.

Badia, S., Bochev, P., Lehoucq, R., Parks, M.L., Fish, J., Nuggehally, M.A., and Gunzburger, M., A force-based blending model forAtomistic-to-continuum coupling, *International Journal for Multiscale Computational Engineering*, vol. **5**, no. 5, pp. 387–406, 2007.

Belytschko, T. and Black, T., Elastic crack growth in finite elements with minimal remeshing, *International Journal for Numerical Methods in Engineering*, vol. **45**, no. 5, pp. 601–620, 1999.

Berlyand, L. and Kolpakov, A., Network approximation in the limit of¶small interparticle distance of the¶effective properties of a high-contrast¶random dispersed composite, *Archive for Rational Mechanics and Analysis*, vol. **159**, no. 3, pp. 179–227, 2001.

Bhattacharjee, S. and Matouš, K., A nonlinear manifold-based reduced order model for multiscale analysis of heterogeneous hyperelastic materials, *Journal of Computational Physics*, vol. **313**, pp. 635–653, 2016.

Cardiff, P. and Demirdžić, I., Thirty years of the finite volume method for solid mechanics, *Archives of Computational Methods in Engineering*, vol. **28**, no. 5, pp. 3721–3780, 2021.

Cardiff, P., Tuković, Ž., Jaeger, P.D., Clancy, M., and Ivanković, A., A lagrangian cell-centred finite volume method for metal forming simulation, *International Journal for Numerical Methods in Engineering*, vol. **109**, no. 13, pp. 1777–1803, 2016.

Carolan, D., Chong, H., Ivankovic, A., Kinloch, A., and Taylor, A., Co-continuous polymer systems: A numerical investigation, *Computational Materials Science*, vol. **98**, pp. 24–33, 2015.

Cavalcante, M.A., Khatam, H., and Pindera, M.J., Homogenization of elastic–plastic periodic materials by FVDAM and FEM approaches – an assessment, *Composites Part B: Engineering*, vol. **42**, no. 6, pp. 1713–1730, 2011.

Cavalcante, M.A., Pindera, M.J., and Khatam, H., Finite-volume micromechanics of periodic materials: Past, present and future, *Composites Part B: Engineering*, vol. **43**, no. 6, pp. 2521–2543, 2012.

Chen, J.S., Pan, C., Wu, C.T., and Liu, W.K., Reproducing kernel particle methods for large deformation analysis of non-linear structures, *Computer Methods in Applied Mechanics and Engineering*, vol. **139**, no. 1-4, pp. 195–227, 1996.

de Borst, R. and Ramm, E. (Eds.), *Multiscale Methods in Computational Mechanics*, Springer Netherlands, 2011.

Dvorak, G.J., On uniform fields in heterogeneous media, *Proceedings of the Royal Society of London. Series A: Mathematical and Physical Sciences*, vol. **431**, no. 1881, pp. 89–110, 1990.

Feyel, F. and Chaboche, J.L., FE2 multiscale approach for modelling the elastoviscoplastic behaviour of long fibre SiC/ti composite materials, *Computer Methods in Applied Mechanics and Engineering*, vol. **183**, no. 3-4, pp. 309–330, 2000.

Fish, J., Bridging the scales in nano engineering and science, *Journal of Nanoparticle Research*, vol. **8**, no. 5, pp. 577–594, 2006.

Fish, J., *Practical Multiscaling*, Wiley, 2013.
URL `https://books.google.hr/books?id=tdCYAAAAQBAJ`

Fish, J., Wagner, G.J., and Keten, S., Mesoscopic and multiscale modelling in materials, *Nature Materials*, vol. **20**, no. 6, pp. 774–786, 2021.

Fish, J., Yuan, Z., and Kumar, R., Computational certification under limited experiments, *International Journal for Numerical Methods in Engineering*, vol. **114**, no. 2, pp. 172–195, 2018.

Fritzen, F. and Böhlke, T., Nonuniform transformation field analysis of materials with morphological anisotropy, *Composites Science and Technology*, vol. **71**, no. 4, pp. 433–442, 2011.

Geers, M.G.D., Kouznetsova, V.G., Matou, K., and Yvonnet, J., 2017. Homogenization Methods and Multiscale Modeling: Nonlinear Problems. American Cancer Society, pp. 1–34.

Ghosh, S. and Moorthy, S., Elastic-plastic analysis of arbitrary heterogeneous materials with the voronoi cell finite element method, *Computer Methods in Applied Mechanics and Engineering*, vol. **121**, no. 1-4, pp. 373–409, 1995.

Glover, K., All optimal hankel-norm approximations of linear multivariable systems and theirL, ∞-error bounds†, *International Journal of Control*, vol. **39**, no. 6, pp. 1115–1193, 1984.

Guo, F., He, B., and Niu, X., Analysis of vapor pressure and void volume fraction evolution in porous polymers: A micromechanics approach, *International Journal of Solids and Structures*, vol. **66**, pp. 133–139, 2015.

Hill, R., On macroscopic effects of heterogeneity in elastoplastic media at finite strain, *Mathematical Proceedings of the Cambridge Philosophical Society*, vol. **95**, no. 3, p. 481494, 1984.

Horstemeyer, M.F., 2009. Multiscale modeling: A review. *Practical Aspects of Computational Chemistry*. Springer Netherlands, pp. 87–135.

Jasak, H. and Weller, H.G., Application of the finite volume method and unstructured meshes to linear elasticity, vol. **48**, no. 2, pp. 267–287, 2000.

Kanouté, P., Boso, D.P., Chaboche, J.L., and Schrefler, B.A., Multiscale methods for composites: A review, *Archives of Computational Methods in Engineering*, vol. **16**, no. 1, pp. 31–75, 2009.

Karabasov, S., Nerukh, D., Hoekstra, A., Chopard, B., and Coveney, P.V., Multiscale modelling: approaches and challenges, *Philosophical Transactions of the Royal Society A: Mathematical, Physical and Engineering Sciences*, vol. **372**, no. 2021, p. 20130390, 2014.

Kouznetsova, V., Geers, M.G.D., and Brekelmans, W.A.M., Multi-scale constitutive modelling of heterogeneous materials with a gradient-enhanced computational homogenization scheme, *International Journal for Numerical Methods in Engineering*, vol. **54**, no. 8, pp. 1235–1260, 2002.

Krysl, P., Lall, S., and Marsden, J.E., Dimensional model reduction in non-linear finite element dynamics of solids and structures, *International Journal for Numerical Methods in Engineering*, vol. **51**, no. 4, pp. 479–504, 2001.

Le, B.A., Yvonnet, J., and He, Q.C., Computational homogenization of nonlinear elastic materials using neural networks, *International Journal for Numerical Methods in Engineering*, vol. **104**, no. 12, pp. 1061–1084, 2015.

Lee, J.D., Li, J., Zhang, Z., and Wang, L., 2017. Sequential and concurrent multiscale modeling of multiphysics: From atoms to continuum. *Micromechanics and Nanomechanics of Composite Solids*. Springer International Publishing, pp. 1–38.

Leonard, M., Murphy, N., Karač, A., and Ivanković, A., A numerical investigation of spherical void growth in an elastic–plastic continuum, *Computational Materials Science*, vol. **64**, pp. 38–40, 2012.

Markl, M. and Krner, C., Multiscale modeling of powder bedbased additive manufacturing, *Annual Review of Materials Research*, vol. **46**, no. 1, pp. 93–123, 2016.

Matouš, K., Geers, M.G., Kouznetsova, V.G., and Gillman, A., A review of predictive nonlinear theories for multiscale modeling of heterogeneous materials, *Journal of Computational Physics*, vol. **330**, pp. 192–220, 2017.

McNamara, D., Alveen, P., Carolan, D., Murphy, N., and Ivanković, A., Micromechanical study of strength and toughness of

advanced ceramics, *Procedia Materials Science*, vol. **3**, pp. 1810–1815, 2014.

McNamara, D., Alveen, P., Damm, S., Carolan, D., Rice, J.H., Murphy, N., and Ivanković, A., A raman spectroscopy investigation into the influence of thermal treatments on the residual stress of polycrystalline diamond, *International Journal of Refractory Metals and Hard Materials*, vol. **52**, pp. 114–122, 2015.

Michel, J. and Suquet, P., Computational analysis of nonlinear composite structures using the nonuniform transformation field analysis, *Computer Methods in Applied Mechanics and Engineering*, vol. **193**, no. 48-51, pp. 5477–5502, 2004.

Mirkhalaf, S., Pires, F.A., and Simoes, R., Determination of the size of the representative volume element (RVE) for the simulation of heterogeneous polymers at finite strains, *Finite Elements in Analysis and Design*, vol. **119**, pp. 30–44, 2016.

Moes, N., Dolbow, J., and Belytschko, T., A finite element method for crack growth without remeshing, *International Journal for Numerical Methods in Engineering*, vol. **46**, no. 1, pp. 131–150, 1999.

Moore, B., Principal component analysis in linear systems: Controllability, observability, and model reduction, *IEEE Transactions on Automatic Control*, vol. **26**, no. 1, pp. 17–32, 1981.

Moulinec, H. and Suquet, P., A numerical method for computing the overall response of nonlinear composites with complex microstructure, *Computer Methods in Applied Mechanics and Engineering*, vol. **157**, no. 1-2, pp. 69–94, 1998.

Paley, M. and Aboudi, J., Micromechanical analysis of composites by the generalized cells model, *Mechanics of Materials*, vol. **14**, no. 2, pp. 127–139, 1992.

Perić, D., de Souza Neto, E.A., Feijóo, R.A., Partovi, M., and Molina, A.J.C., On micro-to-macro transitions for multi-scale analysis of non-linear heterogeneous materials: unified variational basis and finite element implementation, *International Journal for Numerical Methods in Engineering*, vol. **87**, no. 1-5, pp. 149–170, 2010.

Salciccioli, M., Stamatakis, M., Caratzoulas, S., and Vlachos, D., A review of multiscale modeling of metal-catalyzed reactions: Mechanism development for complexity and emergent behavior, *Chemical Engineering Science*, vol. **66**, no. 19, pp. 4319–4355, 2011.

Simo, J. and Hughes, T., *Computational Inelasticity*, Interdisciplinary Applied Mathematics, Springer New York, 2006.

Tadmor, E.B., Ortiz, M., and Phillips, R., Quasicontinuum analysis of defects in solids, *Philosophical Magazine A*, vol. **73**, no. 6, pp. 1529–1563, 1996.

Tong, M., Duggan, G., Liu, J., Xie, Y., Dodge, M., Aucott, L., Dong, H., Davidchack, R.L., Dantzig, J., Barrera, O., Cocks, A.C., Kitaguchi, H., Lozano-Perez, S., Zhao, C., Richardson, I., Kidess, A., Kleijn, C.R., Wen, S., Barnett, R., and Browne, D.J., Multiscale, multiphysics numerical modeling of fusion welding with experimental characterization and validation, *JOM*, vol. **65**, no. 1, pp. 99–106, 2012a.

Tong, M., Liu, J., Xie, Y., Dong, H.B., Davidchack, R.L., Dantzig, J., Ceresoli, D., Marzari, N., Cocks, A., Zhao, C., Richardson, I.,

Kidess, A., Kleijn, C., Hoglund, L., Wen, S.W., Barnett, R., and Browne, D.J., An integrated framework for multi-scale multi-physics numerical modelling of interface evolution in welding, *IOP Conference Series: Materials Science and Engineering*, vol. **33**, p. 012029, 2012b.

Tuković, Ž., Karač, A., Cardiff, P., Jasak, H., and Ivanković, A., OpenFOAM finite volume solver for fluid-solid interaction, *Transactions of FAMENA*, vol. **42**, no. 3, pp. 1–31, 2018.

Tuković, Ž., Wu, K., Cardiff, P., and Ivanković, A., Finite volume multiscale modelling of solid mechanics problems, *4th International Conference on Multi-scale Computational Methods for Solids and Fluids*, Ibrahimbegovi, A. and Hanjalić, K. (Eds.), Faculty of Civil Engineering, University of Sarajevo, 2019.

Wagner, G.J. and Liu, W.K., Coupling of atomistic and continuum simulations using a bridging scale decomposition, *Journal of Computational Physics*, vol. **190**, no. 1, pp. 249–274, 2003.

Weller, H.G., Tabor, G., Jasak, H., and Fureby, C., A tensorial approach to computational continuum mechanics using object-oriented techniques, *Computers in Physics*, vol. **12**, no. 6, p. 620, 1998.

Xiao, S. and Belytschko, T., A bridging domain method for coupling continua with molecular dynamics, *Computer Methods in Applied Mechanics and Engineering*, vol. **193**, no. 17-20, pp. 1645–1669, 2004.

Yashchuk, I., 2018. A multiscale finite element framework for additive manufacturing process modeling. Master's thesis, Aalto University. School of Engineering.

Yvonnet, J. and He, Q.C., The reduced model multiscale method (r3m) for the non-linear homogenization of hyperelastic media at finite strains, *Journal of Computational Physics*, vol. **223**, no. 1, pp. 341–368, 2007.

Zeng, Q. and Qin, Y., 2018. Multiscale modeling of hybrid machining processes, *Hybrid Machining*. Luo, X. and Qin, Y. (Eds.). Academic Press, pp. 269–298.

(a)

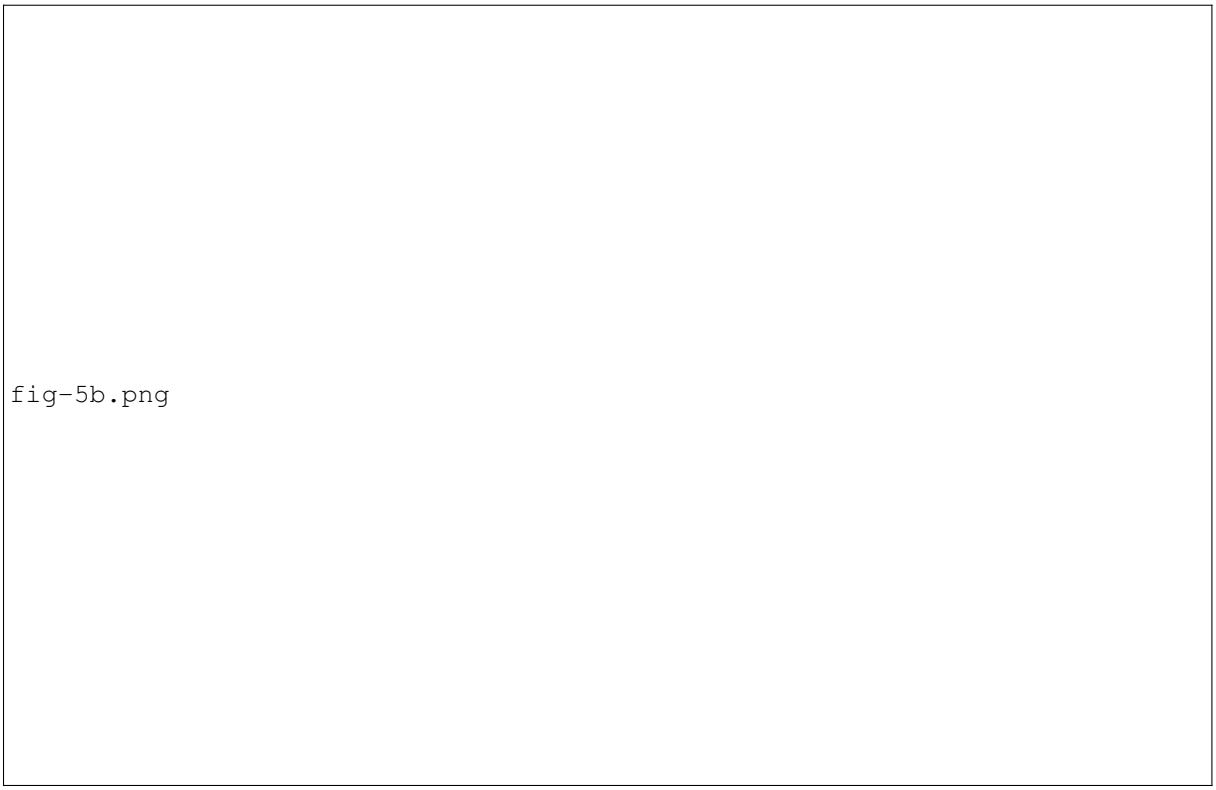

(b)

FIG. 5: Finite volume mesh for perforated plate without/with large central hole: (a) single-scale analysis; (b) macro domains and RVE for two-scale analysis.

(a)

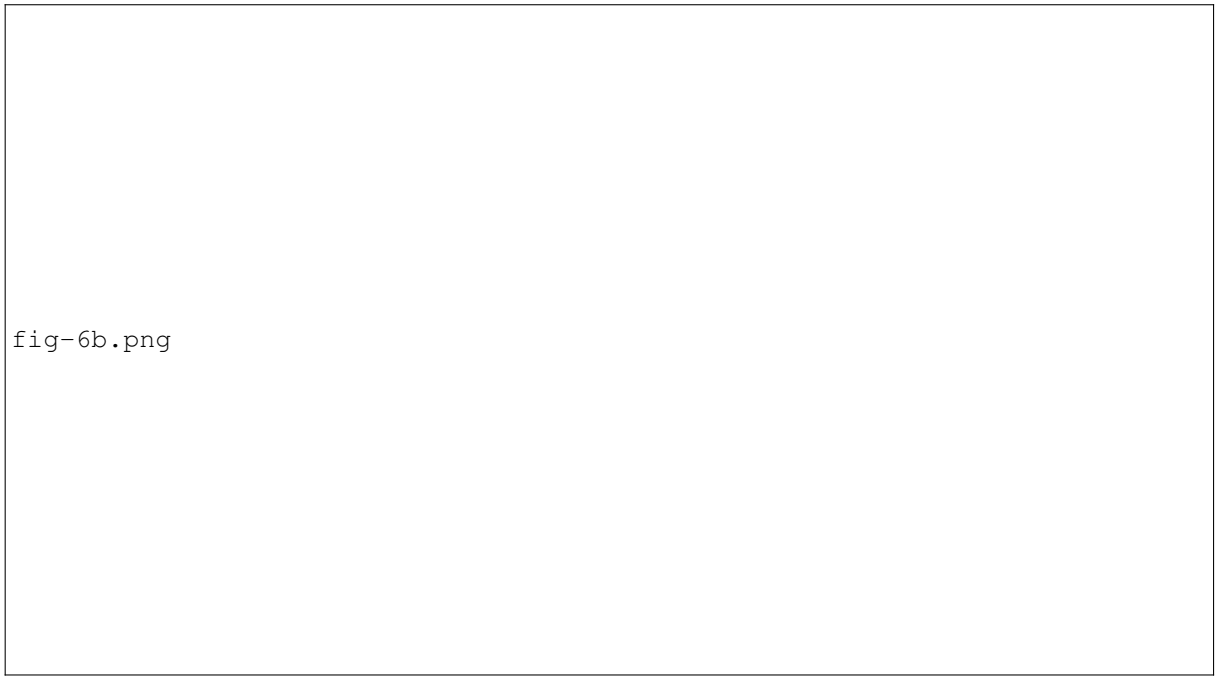

(b)

FIG. 6: Distribution of displacement component in the loading direction in the single-scale analysis and two-scale analysis with an RVE near to the bottom-left of the plate for: (a) uniform, perforated plate, (b) plate with large central hole.

(a)

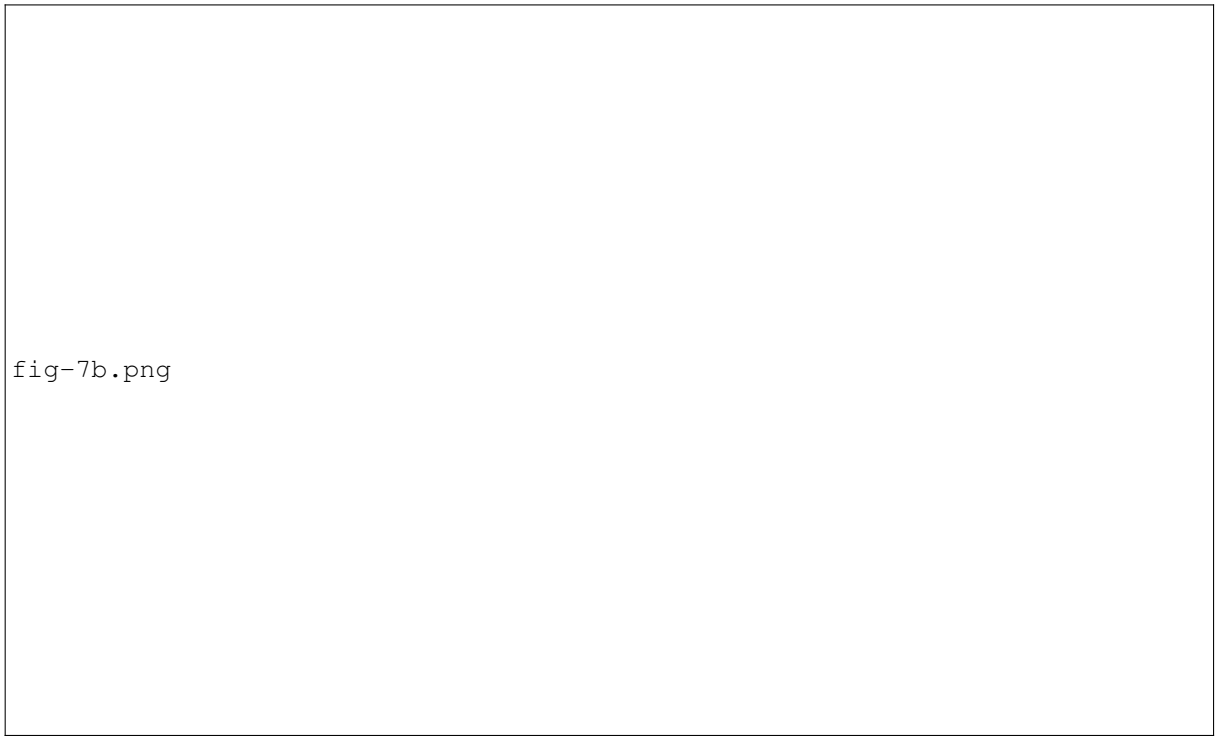

(b)

FIG. 7: Distribution of stress in the loading direction in the single-scale analysis and two-scale analysis with an RVE near to the bottom-left of the plate for: (a) uniform, perforated plate, (b) plate with large central hole.

(a)

(b)

FIG. 8: Comparison between stress-displacement curves from the single-scale and two-scale analyses for (a) the uniform perforated plate without a central hole and (b) the perforated plate with a central hole.

FIG. 9: Finite volume meshes for 3D perforated plate without central hole: (a) single-scale analysis; (b) macro domain and RVE (not to scale) for two-scale analysis.

FIG. 10: Stress-displacement curves for single-scale analysis and two-scale analysis of the uniform, perforated plate from 2D and 3D simulations.

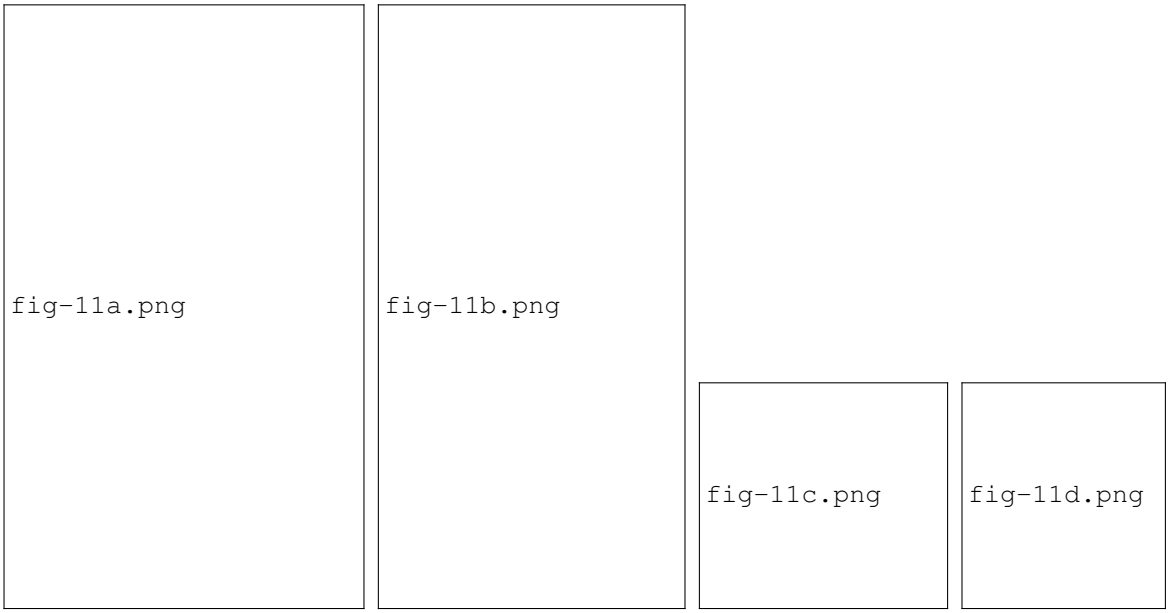

FIG. 11: 3D geometry in (a) single-scale analysis, (b) sectional view of 3D geometry, (c) 3D RVE in two-scale analysis, and (d) sectional view of 3D RVE.

FIG. 12: Stress-displacement curves for single-scale analysis and two-scale analysis of the perforated plate without large central hole in 2D and full 3D.